ACS Energy LETTERS

Cite This: ACS Energy Lett. 2019, 4, 2748−2756

http://pubs.acs.org/journal/aelccp

LETTER

Dual-Source Coevaporation of Low-Bandgap $FA_{1-x}Cs_xSn_{1-y}Pb_yI_3$ Perovskites for Photovoltaics

James M. Ball, Leonardo Buizza, Harry C. Sansom, Michael D. Farrar, Matthew T. Klug, Juliane Borchert, Jay Patel, Laura M. Herz, Michael B. Johnston,* and Henry J. Snaith*

Department of Physics, University of Oxford, Clarendon Laboratory, Parks Road, Oxford, OX1 3PU, United Kingdom

Supporting Information

ABSTRACT: Perovskite halides are well-suited to monolithic multijunction photovoltaics, promising low-cost solar-to-electrical power conversion. Critical to all-perovskite multijunction fabrication is the deposition of a low-bandgap absorber without damaging other device layers. Vapor deposition is thus an attractive method, obviating the need for optically lossy protective interlayers, but is challenging for multicomponent perovskites. Here, we demonstrate a method to dual-source coevaporate low-bandgap perovskite films and devices. We used mixtures formed by melting of metal halides as a single-crucible source of Cs, Pb, and Sn cations. Surprisingly, when this melt was coevaporated with formamidinium iodide (FAI), uniform and dense perovskite films in the family $FA_{1-x}Cs_xSn_{1-y}Pb_yI_3$ were formed. Inclusion of SnF_2 in the melt helped to regulate the perovskite's optoelectronic quality, leading to a steady-state power conversion efficiency of ∼10% in a solar cell. This represents a new processing paradigm for evaporated perovskite alloys, which is an important step toward all-perovskite multijunction photovoltaics.

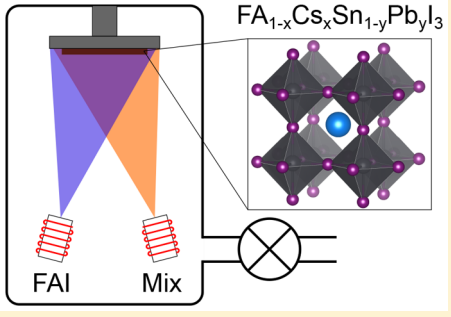

The power conversion efficiencies obtained from single-junction solar cells based on ABX_3 perovskite halides[1,2] are fast approaching the benchmark of crystalline Si.[3] However, as these cells approach their thermodynamic efficiency limits, further improvements become increasingly difficult to achieve. An established method for surmounting this bottleneck is the multijunction cell architecture that can reduce photon energy losses due to carrier thermalization.[4] Metal halide perovskites are a very attractive prospect for multijunction cells because their junctions are highly efficient and can potentially be processed cheaply under mild conditions that do not degrade predeposited layers in the device stack.[5,6]

Perovskite−Si tandems solar cells have recently surpassed the efficiency of single-junction crystalline Si cells,[3] but all-perovskite multijunction cells could potentially offer higher power conversion efficiencies at lower cost.[7−9] Recent analysis of the optical and electronic properties of all-perovskite devices incorporating state-of-the-art materials suggests that efficiencies beyond 32% are realistically achievable in the near future.[10] There are several challenges to achieving this, but chief among them is the ability to deposit a stable, low-bandgap perovskite thin film onto an existing wide-bandgap perovskite junction in a layer stack that minimizes optical losses to parasitic absorption.

The most promising low-bandgap perovskite compositions are alloys with both Pb and Sn in the B-site,[9,11−13] which exhibit reduced bandgaps compared to either of their single-metal analogues.[12,14] Sn^{2+} is well-known to be highly unstable to oxidation to Sn^{4+} by atmospheric oxygen, but fortunately, the rate of oxidation is dramatically reduced when alloyed with Pb due to a fundamental change in the reaction pathway.[15] This renders the alloys more stable than would be expected based on their tin content.

Alloys in this family have recently exhibited high efficiencies of >21 and >24% in solution-processed single-junction and monolithic tandem devices, respectively.[16] However, these efficiencies have only been reached using a relatively less stable A-site site mixture comprised of formamidinium and methylammonium. To ensure that the perovskite is thermally and structurally stable under operating conditions, this system requires a mixture of formamidinium ($NH_2CHNH_2^+$, FA) and Cs at the A-site.[9,17] Therefore, a mixed A- and B-site multication perovskite, in the family $FA_{1-x}Cs_xSn_{1-y}Pb_yI_3$, should be among the leading candidates for stable, low-bandgap junctions and has already been shown to exhibit

Received: August 23, 2019
Accepted: October 10, 2019
Published: October 10, 2019

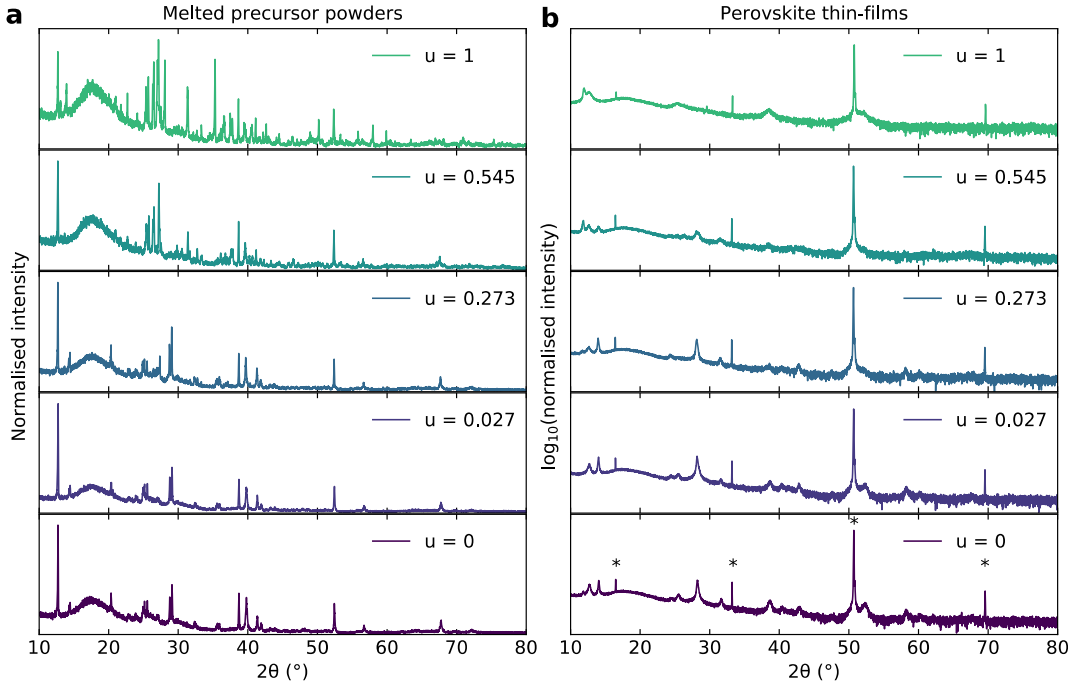

Figure 1. (a) **Normalized powder XRD spectra of ground precursor mixtures after melting for different SnF_2 ratios, *u*.** (b) **Normalized XRD spectra plotted on a log scale of perovskite thin films formed by dual-source coevaporation of FAI with melted precursor mixtures with different SnF_2 ratios, *u*. Peaks corresponding to the z-cut quartz substrates are highlighted with asterisks for $u = 0$. In both figures, the 2θ angle corresponds to the $K\alpha_1$ wavelength of the Cu X-ray source.**

promising efficiencies of ∼15% in solution-processed solar cells.[9,11]

One technique for perovskite deposition that can be nondestructive to pre-existing layers is vacuum evaporation, which has been used successfully to fabricate perovskite solar cells with high efficiencies.[18,19] Additionally, this method could obviate the need for optically lossy interlayers between the junctions. These interlayers have previously been required to protect the front cell against degradation during subsequent layer deposition by solution processing[7,9] but contribute significant optical losses.[10]

However, multication systems are somewhat challenging to form via vapor deposition because, conventionally, the relatively large number of precursor materials (CsI, PbI_2, SnI_2, FAI, plus additives) requires multiple sources, increasing the complexity of process control.[20,21] An alternative that we propose here is to use unconventional metal halide mixtures that can be evaporated from a single crucible as the source for Cs, Pb, Sn and halide. These metal halide mixtures can be formed in a melt reaction of conventional precursors and then subsequently coevaporated with formamidinium iodide (FAI), thus requiring only two evaporation sources to form the multicomponent perovskite alloys. The resulting films that we have produced are mixed A- and B-site multication perovskites in the family $FA_{1-x}Cs_xSn_{1-y}Pb_yI_3$. Furthermore, we have found that incorporating SnF_2 as a processing substituent in the precursor mixture helps to control the formation of impurity phases in the evaporated perovskite thin films, leading to improved optoelectronic quality and steady-state power conversion efficiencies approaching 10% in solar cells. Further optimization of this process offers a practical route to highly efficient all-perovskite tandem solar cells fabricated by vapor deposition.

Our precursor mixtures that comprise the source of Cs, Pb, Sn, and some I in the resulting perovskites were formed in a melt reaction of conventional perovskite precursors: CsI, PbI_2, SnI_2, and SnF_2. To determine the ratios of these precursors for use in the mixture, we made several considerations based on existing literature. The Cs molar fraction in the A-site, *x*, was chosen to be 0.25 as it has previously been shown to benefit the thermal stability of the resulting perovskite.[9] The bandgap minimum in the Pb−Sn series occurs when they are roughly equimolar in the B-site. We chose the Sn molar fraction in the B-site, *y*, to be 0.55 as a reasonable starting point. Incorporating SnF_2 into the precursor mixture in solution-processed Sn and mixed Pb−Sn perovskites has been shown to be important for high power conversion efficiency partly because, as a reducing agent, it helps to inhibit oxidation of Sn^{2+} to Sn^{4+}.[12,22] Additionally, it may be beneficial for both crystallization/film formation and grain boundary passivation.[12] To maintain the aforementioned Pb:Sn stoichiometry, SnF_2 was incorporated substitutionally with SnI_2. The molar fraction of SnI_2 to SnF_2, $0 \leq u \leq 1$, was varied to determine its effect on the power conversion efficiency of solar cells.

The metal halides were ground into powders and heated in a crucible under inert atmosphere above the melting points of PbI_2, SnI_2, and SnF_2 and then allowed to cool naturally to room temperature. The expected reaction is therefore

$$5CsI + 9PbI_2 + 11[(1-u)SnI_2 + uSnF_2] \rightarrow \sum_i \{Pb_{1-a}Sn_a(I_{1-b}F_b)_2\}_i + \sum_j \{CsPb_{1-c}Sn_c(I_{1-d}F_d)_3\}_j \quad (1)$$

where $0 \leq a, b, c, d \leq 1$. Predicting the products of this reaction precisely is difficult because there are many known stable possibilities, some with multiple crystallographically metastable phases at room temperature. This includes known

DOI: 10.1021/acsenergylett.9b01855
ACS Energy Lett. 2019, 4, 2748−2756

single-phase alloys where both the metal and halogen atoms can be mixed.[23,24] However, due to the excess of metal dihalide reactants, it could at least be expected that Cs will be consumed in one or more $CsPb_{1-c}Sn_c(I_{1-d}F_d)_3$ phases, leaving one or more $Pb_{1-a}Sn_a(I_{1-b}F_b)_2$ products, the ratios of which should depend on the SnF_2 fraction, u.

To more precisely determine the composition of the ingots after the melt reaction, we measured the X-ray diffraction (XRD) patterns of their powders, as shown in Figure 1, and analyzed them using Pawley fitting to attempt to assign the unit cells of known materials, as shown in Figure S2. The powder diffraction patterns of the mixtures of ground precursors before melting along with Pawley fits are shown in Figure S1. The XRD patterns before melting are as expected: all peaks can be accounted for as originating from the constituent metal halide phases, showing that no reactions have taken place. However, after melting, significant changes can be observed. For values of the SnF_2 fractions u = 0 and 0.027, we found that the Cs was all contained in a phase with the same symmetry as γ-$CsSnI_3$, which is a 3D perovskite black phase (space group *Pnma*).[25] For u = 0.273, Cs was again all contained in ternary phases, but in addition to the γ-$CsSnI_3$-like phase, a phase with the symmetry of δ-$CsSnI_3$ was formed, which is a nonperovskite yellow phase (space group *Pnam*) with 1D chains of edge-sharing Pb/Sn−I octahedra.[26] For higher values of u, there was a significant fraction of this δ-phase but without the γ-phase. In addition, the sample where u = 0.545 contained some peaks that were too small to index, and the sample where u = 1 contained a phase that we were able to index but not identify as a known phase. This phase was in the space group *Pnam* and with unit cell dimensions of a = 8.613(1) Å, b = 8.6576(8) Å, and c = 12.7077(6) Å. The space group and unit cell are consistent with those of a 3D perovskite phase but with lattice parameters significantly different from those of γ-$CsSnI_3$ (a = 8.68800 Å, b = 8.64300 Å, c = 12.37800 Å, space group *Pnma*)[25] and γ-$CsPbI_3$ (a = 8.85610 Å, b = 8.57660 Å, c = 12.47220 Å, space group *Pnam*).[27] All compositions exhibited an additional phase consistent with the symmetry of PbI_2, but SnI_2, SnF_2, and CsI could not be detected after melting. Due to the complex nature of the multiphasic XRD patterns, the convoluted peaks meant that reliable lattice parameters could not be extracted. Therefore, the extent of Pb/Sn or I/F mixing in all of the identified phases requires further exploration beyond the present scope.

The melted precursor mixtures were subsequently evaporated from a single source to form thin films that were analyzed by XRD. The thin-film spectra are shown in Figure S4 in comparison to the precursors PbI_2, SnI_2, and SnF_2. We found that the peak positions for thin films of SnI_2 showed stronger agreement with the hexagonal phase as opposed to the monoclinic phase that usually dominates the powder form, as has been observed previously.[28] All of the thin films show a small number of sharp peaks, suggesting that they are highly oriented and crystalline and with symmetries that cannot be distinguished from PbI_2 or SnI_2 in its hexagonal phase. There are small shifts in the main peak positions, as highlighted in Figure S5. There is also some peak broadening as u increases. This may be a result of reduced crystallinity, two or more overlapping crystalline phases, and/or alloying of the metals/halides. Some samples exhibited two additional low-intensity broad peaks at ∼28 and ∼44°. These correspond to the 110 and 210 reflections of cubic CsI.[29]

The UV−vis−NIR absorption and steady-state photoluminescence (PL) spectra of the precursor thin films, formed by evaporation of the melted precursor mixtures onto quartz substrates, are shown in Figure S14. All of the films show clear absorption onsets at wavelengths ≤ 550 nm. At higher wavelengths, the reflectance and transmittance spectra exhibit undulations mostly caused by thin-film interference, highlighting the smoothness of the evaporated layers. Where $u \leq$ 0.273, the films exhibit red-shifted absorption onsets compared to both PbI_2 and SnI_2, which in this case is in a yellow-phase, consistent with its XRD spectrum.[28]

The PL emission spectra for the mixed precursor films all have their most intense peak centered at ∼515 nm, which is accompanied by a small shoulder below 500 nm. These peaks are slightly red-shifted compared to PbI_2, which exhibits its peak emission at ∼510 nm. The appearance of a shoulder in the emission spectra of the precursor mixture films, combined with the red shifts in the absorption spectra, is indicative of filtering by reabsorption. Therefore, we conclude that the emission most likely comes from PbI_2 that remains unreacted in the films following evaporation of only the metal halide mixture. None of the samples that exhibited red-shifted absorption onsets showed correspondingly red-shifted PL. This implies that either the PL efficiency from the absorption edge is very low and/or nonradiative recombination pathways are more likely for photoexcited carriers. Indeed, some of the films show emission peaks at significantly lower energies than the absorption onset, which could be due to either recombination centers or impurity phases. Surprisingly, we found that this was also true of pure SnI_2. The emission wavelengths are not consistent with either $CsPbI_3$ or $CsSnI_3$ in their black phases.[25,27] For the emission to arise from impurity phases, these phases must be poorly crystalline/amorphous, have closely matching XRD spectra to the majority phase, or be in such low weight ratios so as not to be detectable by XRD. There are no features in the absorption spectra corresponding to the lower-energy emission. This suggests that the species emitting at lower energies constitute a small fraction of the overall film composition.

Following characterization of the precursors, thin films of perovskites were deposited by dual-source coevaporation under vacuum with the melted mixtures in one source and FAI in another. There was no thermal annealing step after deposition. Figure 1 presents their XRD patterns, Figure S3 shows Pawley fits, and the region where $2\theta \leq 15°$ is highlighted in Figure S6. The Pawley fits suggest that the SnF_2 fraction, u, has a significant impact on which phases are formed in thin films. In general, for low ratios of SnF_2 where $u \leq$ 0.273, the majority phase is a black 3D perovskite phase with the same symmetry as α-$FASnI_3$ (space group *Amm*2).[30] However, increasing the SnF_2 ratio toward complete replacement of SnI_2 leads to the formation of a yellow 1D nonperovskite phase with the same symmetry as δ-$FAPbI_3$ (space group *P*63*mc*).[30] All films exhibited a minority PbI_2 or SnI_2 impurity phase, whose peak intensities were lowest for u = 0.273.

The stoichiometries of Cs, Pb, and Sn in the evaporated perovskite films were determined by inductively coupled plasma mass spectroscopy (ICP-MS). We found that the stoichiometries of the films deviated significantly from the elemental ratio in the precursor mixture, with a weak dependence on the SnF_2 content. We found all of the films to be very Sn-rich with a B-site content of >95%. This is

DOI: 10.1021/acsenergylett.9b01855
ACS Energy Lett. 2019, 4, 2748−2756

significantly higher than would be expected if the precursor mixtures evaporated homogeneously. The Cs content relative to the B-site was ~3% for $u \leq 0.273$ and in the range of 5−7% for higher values of u. These values are lower than would be expected if the precursor mixture evaporated homogeneously, implying predominantly FA in the A-site. The Cs ratio makes a step increase between $u = 0.273$ and 0.545. We note that it was not possible to determine the C, H, N, and I stoichiometry using this technique. A summary of the measurements is shown in Table S1, and the stoichiometries derived from them are summarized in Table S2.

The UV−vis−NIR absorption coefficient spectra of the perovskite films, shown in Figure 2, reveal further information

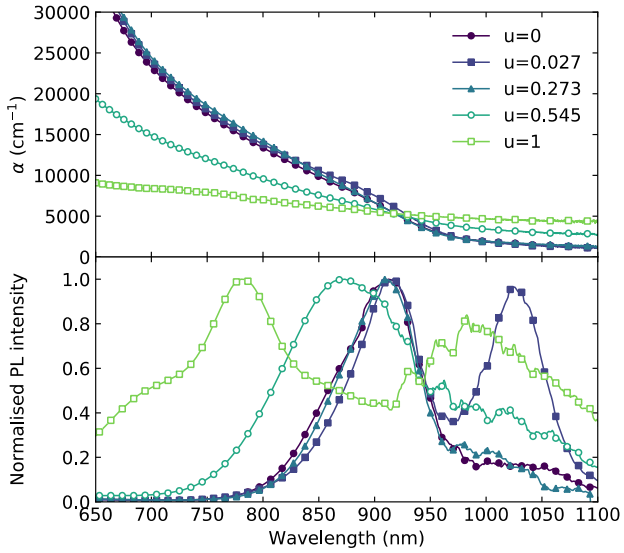

Figure 2. Absorption coefficient, α, (top) and normalized PL (bottom) spectra near the absorption edge of $FA_{1-x}Cs_xSn_{1-y}Pb_yI_3$ perovskite thin films on quartz. PL was obtained using a 400 nm continuous wave laser with an intensity of 1.27 W/cm^2 for excitation. The legend indicates different values of the SnF_2 fraction, u. Markers in the absorption spectra indicate every 75th data point, whereas markers in the PL spectra indicate every 10th data point. $\alpha = A/d$, where absorbance $A = -\ln(T/(1 - R))$, d is film thickness, T is transmittance, and R is reflectance.

about their composition. For lower values of the SnF_2 fraction u, the films exhibit a broad absorption edge with an onset at ~950 nm. However, for the higher values of u, the absorption edge in the near-IR could not be resolved. Instead a broad blue-shifted shoulder appears. The bandgaps of the films that showed characteristic perovskite absorption spectra were estimated by fitting their absorption coefficients in Tauc[31] plots (shown in Figure S22 and summarized in Table S6) and with Elliot's model[32,33] (as shown in Figure S23 and summarized in Table S7). The fits suggest that the perovskites have bandgaps of ≤1.34 eV, slightly lower than the PL peak energies (shown in Figure 2 and summarized in Table S6). The value of u seems to have little impact on the band-edge position in the lower range. The Elliot model fits yielded relatively low exciton binding energies compared to Pb-based perovskites,[34] in the range 1−8 meV, as has been observed previously in Sn-based perovskites.[22]

The steady-state PL spectra arising from photoexcition at 400 nm are also shown in Figure 2. For $u \leq 0.273$, the PL emission peaks overlap with the broad absorption edge. The peak wavelengths are summarized in Table S6. For $u = 0.027$, there is an additional red-shifted emission peak with an energy below the absorption onset that could be due to either a recombination center or an impurity phase. With no corresponding low-energy absorption edge, this could be a minority perovskite phase with a different Pb/Sn ratio, closer to the achievable bandgap minimum. Films with higher values of u have the most intense emission from a blue-shifted peak compared to films with lower values of u, commensurate with emission from a different stoichiometry perovskite.

The PL lifetimes for these films were measured using time-correlated single-photon counting after photoexcition at 400 nm with fluences of 53 and 420 nJ/cm^2, as shown in Figure S17. The lifetimes are summarized in Figure S16a. In general, the lifetime at the PL peak slowly decreases with increasing SnF_2 fraction u, except for $u = 0.027$, which exhibited an increased lifetime of >15 ns. The lifetimes for the other compositions are all below 10 ns.

We also performed time-resolved THz photoconductivity using a pump wavelength of 800 nm to measure the effective charge-carrier mobility in these perovskite thin films. The effective mobilities derived from these measurements are summarized in Figure S16a. For $u \leq 0.273$, the mobilities are quite similar, in the range of 12−15 cm^2/(V s). These values are close to those previously reported for both pure Sn and Pb−Sn alloy perovskites using the same measurement technique.[7,35] However, for higher values of u, the mobility drops off sharply. Combined with the PL lifetime data, we can estimate the charge-carrier diffusion lengths, which are summarized in Figure S16b. Films in the highest mobility range exhibit diffusion lengths in the range of 400−700 nm, comparable to or greater than the corresponding film thicknesses, which are summarized in Table S5 (as measured using profilometry). In the lower mobility range, the diffusion lengths drop below the film thicknesses.

Having determined that we were able to form low-bandgap perovskite films with reasonable optoelectronic quality, we proceeded to fabricate solar cells. These solar cells based on the evaporated perovskite films were fabricated in a p−i−n architecture using poly(3,4-ethylenedioxythiophene) polystyrenesulfonate (PEDOT:PSS) as the hole-selective contact and a bilayer of phenyl-C61-butyric acid methyl ester (PCBM) and bathocuproine (BCP) as a combined electron-selective contact. A device cross section, imaged by scanning electron microscopy (SEM), is shown in Figure 3a, which highlights the layers of the device stack and the uniformity and density of the evaporated perovskite layer. Longer-range cross sections, highlighting the uniformity of this evaporated film, are shown in Figure S7. Top-view SEM images of the devices outside of the top electrode region reveal that all of the perovskite films have relatively small grain sizes, as is commonly observed with evaporated perovskites.[18−21,36,37] An example is shown in Figure 3b. Additional top-view images for films with each SnF_2 fraction u are shown in Figures S8−S13. Estimates of the grain size distributions based on image analysis (Figures S8−S13) indicate that the grain sizes mostly fall in the range from 10 nm to a few hundred nm, fairly independently of u.

The best current density−voltage (J−V) scans under simulated AM1.5G illumination for each SnF_2 fraction u are shown in Figure 4a, while statistics for the best-performing batch of devices are given in Figure S19. The performance parameters for the champion devices of each composition are

DOI: 10.1021/acsenergylett.9b01855
ACS Energy Lett. 2019, 4, 2748−2756

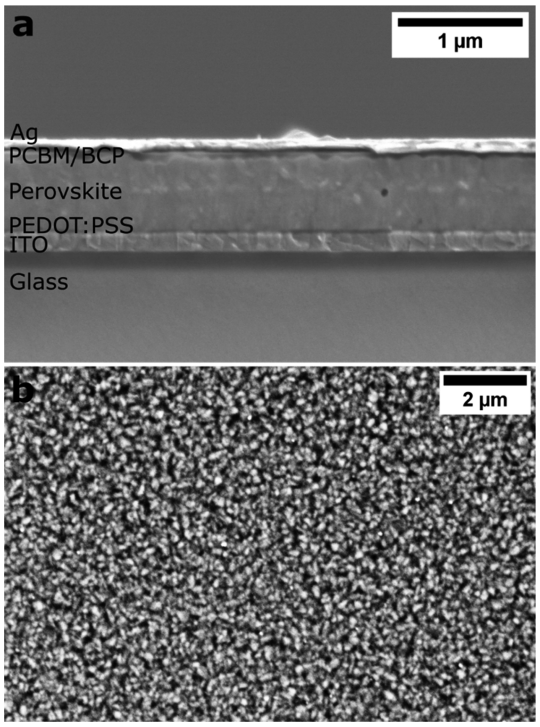

Figure 3. SEM images of the best-performing device in (a) cross section (highlighting the layers in the device structure) and (b) top-view (outside of the top electrode area).

summarized in Table S3. For most values of u, the devices exhibit characteristic photovoltaic behavior. With an intermediate u value, the device performance is maximized to a scanned efficiency of ∼11.5% in the forward direction, predominantly due to a significant increase in short-circuit current density (J_{SC}), up to ∼20 mA/cm^2, compared to the other compositions. The steady-state power outputs (SPOs) at the maximum power point voltage from the $J-V$ scans of some example devices are shown in Figure S20. The performance parameters are summarized in Tables 1 and S4. The champion device shows a small decrease in SPO over 50 s to approximately ∼9.3% power conversion efficiency, as shown in Figure 4b. The open-circuit voltage (V_{OC}) and fill factor (FF) of the best device are around 0.78 V and 0.74, respectively. The cells exhibit some hysteresis between the forward (V_{OC} to J_{SC}) and reverse (J_{SC} to V_{OC}) $J-V$ scans, as is often observed in perovskite-based solar cells.[38] Annealing the perovskite films immediately after evaporation generally resulted in lower device performance.

The origin of the measured trend in J_{SC} in the $J-V$ characterization is revealed more clearly in the external quantum efficiency (EQE) spectra shown in Figure 4c. The integrated J_{SC}'s based on the EQE spectra and the AM1.5G solar spectrum agree with the measured values under the solar simulator to within ∼10% and are summarized in Figure S21 and in Figure 4d for the champion composition. For lower values of the SnF_2 fraction u, current generation in the blue region of the excitation spectrum is low. The EQE increases in this spectral region for increasing u, up to the champion composition, before dropping again. An example spectrum of the absorptance (1 − reflectance, R) of a device made with the champion composition is shown in Figure 4d. This spectrum shows that the device absorbs most incident light relatively uniformly across the spectrum below the bandgap. Interestingly, this EQE profile is consistent with a very short electron diffusion length in this material; free electrons generated from light absorbed close to the p-type collection electrode struggle to diffuse across the entire film thickness to contribute to current in the external circuit.[40]

The effective device bandgaps,[41] defined as the maxima of the derivatives d(EQE)/dE, where E is the photon energy, are shown in Figure S21 and summarized in Table S8. For values of the SnF_2 fraction where $u \leq 0.454$, the effective bandgaps are blue-shifted by a few 10s of meV compared the values extracted from optical measurements of the bare films and are in the range of 1.34−1.43 eV. For $u = 1$, the effective bandgap is significantly blue-shifted compared to the other compositions to 1.56 eV.

Solution-processed control samples were made with the same ratio of Cs:Sn:Pb in the precursor solution as found in the champion device ($u = 0.273$) by ICP-MS, where SnF_2 was incorporated at a commonly used ratio[9] (10 mol %) either substitutionally or in excess of SnI_2. Their effective device bandgaps of 1.36 eV, shown in Figure S27, were nearly identical to that of the champion evaporated device, 1.37 eV. These values were blue-shifted by 70−80 meV compared to a previously reported device where the Cs:Sn:Pb ratio was 25:50:50 ($FA_{0.75}Cs_{0.25}Pb_{0.5}Sn_{0.5}I_3$), as shown in Figures 4c and S28.[7] Indeed, Eperon et al. reported that bandgaps > 1.3 eV are consistent with films that have a higher Sn content.[7] Additional characterization and discussion of these samples is given in section S11.

On the basis of the effective device bandgaps of the evaporated samples in the present work, the V_{OC}'s in the radiative limit and the effective electroluminescence quantum yields (η_{EL}) can be estimated and are summarized in Table S8. The device composition with the lowest V_{OC} loss (highest V_{OC}) has an effective η_{EL} on the order of ∼10^{-3}%. The other compositions have effective η_{EL}'s 1−3 orders of magnitude lower.

We have shown here that it is possible to deposit dense and uniform perovskite alloy films with mixed A- and B-site cations using dual-source coevaporation. These can be used in solar cells with promising power conversion efficiencies. The device performance seems to correlate with the film composition, particularly the quantity of impurity phases, which can be controlled by tuning the fraction, u, of SnF_2 as the Sn source in the precursor mixture.

The grain sizes that we observed were small compared to some perovskite films formed by solution processing, but they were comparable to other evaporated perovskite films that exhibit good power conversion efficiencies in devices.[19,36] Nevertheless, postdeposition treatments that have been shown to increase grain sizes and enhance device efficiencies, such as exposure to methylammonium chloride vapor,[9] may be promising routes toward improved device performance in the future.

One curious feature in the characteristics of our devices was a deficit in the expected J_{SC}. A well-optimized laboratory device with an effective bandgap of 1.37 eV, as we observed for our champion composition, should be able to generate ∼30−31 mA/cm^2 under AM1.5G solar irradiation assuming a 10% optical loss to reflection and parasitic absorption. However, the highest J_{SC} that we observed here was closer to ∼20 mA/cm^2. The EQE and absorption spectra shown in Figure 4d indicate that, even for the champion composition, a significant portion of this deficit comes from the blue region

DOI: 10.1021/acsenergylett.9b01855
ACS Energy Lett. 2019, 4, 2748−2756

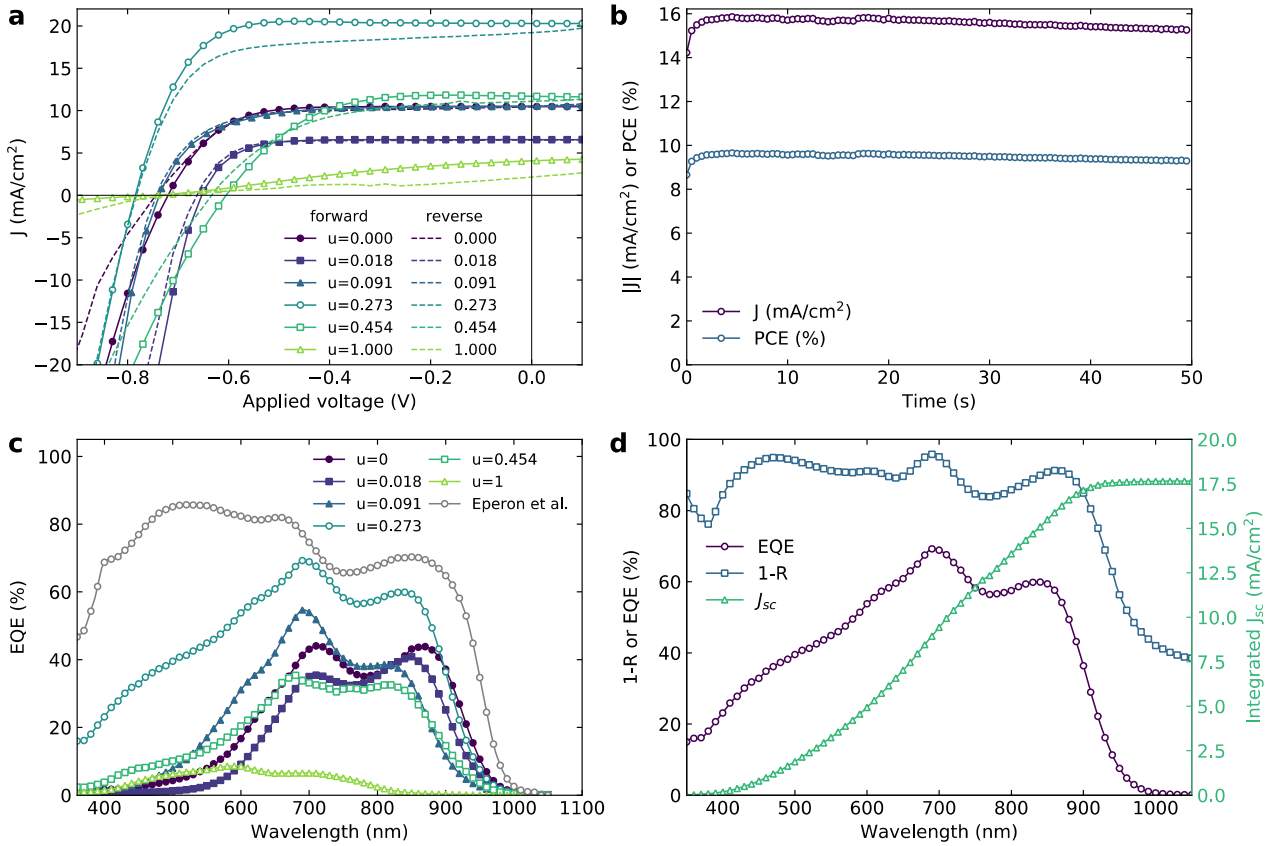

Figure 4. Device characterization. (a) $J-V$ characteristics of the best devices for each value of the SnF_2 fraction u as indicated in the legend. Solid lines with symbols show the forward scan direction (V_{OC} to J_{SC}), and dashed lines show the reverse scan direction (J_{SC} to V_{OC}). (b) Current density and power conversion efficiency at constant voltage (maximum power point voltage from the corresponding $J-V$ scan) as a function of time. (c) EQE spectra for representative devices from the same batch of cells for each value of u as indicated in the legend, compared to digitized[39] data published by Eperon et al. for solution-processed $FA_{0.75}Cs_{0.25}Pb_{0.5}Sn_{0.5}I_3$.[7] (d) Comparison of the EQE and $1 - R$ spectra for the best-performing composition, along with the integrated J_{SC} that would be expected under AM1.5G illumination.

Table 1. Summary of Champion Cell Forward Scan Performance Parameters

u	J_{SC} (mA/cm²)	V_{OC} (V)	FF	PCE (%)	SPO PCE (%)
0	10.48	0.72	0.70	5.10	4.12
0.018	6.51	0.66	0.76	3.19	3.17
0.091	10.52	0.74	0.67	5.14	5.28
0.273	20.29	0.78	0.74	11.48	9.29
0.454	11.69	0.60	0.58	4.03	3.43
1	4.06	0.75	0.32	0.83	0.53

where there is strong absorption but moderate collection efficiency. For other SnF_2 fractions, photocurrents are further suppressed in the blue region. This reduction coincides with a greater portion of yellow impurity phases in the films, as observed by XRD. This could imply that the inclusion of impurities leads to parasitic absorption: light is absorbed by the impurity phases but photogenerated charges cannot be collected. Nevertheless, the calculated bulk diffusion lengths based on charge-carrier mobilities and PL lifetimes for lower values of u suggest that photogenerated carriers should be collected efficiently. This may be indicative of grading of the perovskite composition where, although the bulk composition has sufficient optoelectronic quality, the front interface region with the hole-selective contact could be less pure and thus more detrimental for carrier collection from blue photoexcitation. However, we note that THz photoconductivity measurements yield the sum mobility of both electrons and holes. It is therefore possible that there is a large mismatch between the two mobilities and collection of one carrier limits current extraction. In this case, electrons are most likely to be limiting during blue absorption because they must travel farther for collection. For higher values of u, the diffusion lengths drop below the film thicknesses mainly due to a sharp reduction in mobility. This is most likely related to the reduction in crystallinity of the perovskite phase. Because the Sn-based perovskites are generally expected to be p-type in nature, it is not surprising that the minority carrier, the electron, will be the species that limits long-range diffusion.

The most important compositional effect of the SnF_2 fraction u seemed to be on balancing the formation of different crystalline phases formed within the precursor melts and coevaporated perovskite films, rather than on stoichiometry. When u was too high, a phase with the symmetry of yellow δ-$CsSnI_3$ was prevalent in the precursor mixture, which resulted in perovskite films with an excess of an impurity phase with the symmetry of δ-$FAPbI_3$. This is surprising given how little Pb goes into the film. One possible explanation is that these films were iodine-deficient and contained mostly amorphous SnF_2. When u was too low, a phase with the symmetry of black γ-$CsSnI_3$ was prevalent in the precursor mixture, which resulted in perovskite films with an excess of an impurity phase with the symmetry of PbI_2. However, in this regime, a moderate SnF_2 fraction led to minimization of the

DOI: 10.1021/acsenergylett.9b01855
ACS Energy Lett. 2019, 4, 2748−2756

impurity fraction. This could be an effect of variations of the precursor masses in the starting mixture leading to different effective rates of deposition. SnF_2 may also play additional roles as a Sn source to compensate for mass losses in the oxidation of SnI_2 to SnI_4 or as a reducing agent that drives the reaction back toward SnI_2.[12] One way to test this could be to portion it in excess SnI_2, as is common in solution-processed approaches,[12] rather than substitutionally.

The stoichiometries of the perovskite films formed here deviate somewhat from the elemental ratios in the precursor mixtures, leading to relatively Sn-rich and Cs-deficient films. The discrepancy between the precursor powder and film compositions suggests that the elements in the mixture still have different sublimation rates at a given temperature. Indeed, it is possible that deposition of the constituent elements is incongruent, leading to a graded composition profile, which is the topic of further study. We believe that by carefully controlling the ratio of melt reaction products in the evaporation crucible it should be possible to tune the elemental sublimation rates at a given temperature and hence control the stoichiometry of the final perovskite film. This is the subject of ongoing work. Nevertheless, on the basis of the obtained stoichiometries, the device performances shown here compare very favorably to previous reports using Pb-free Sn-based absorbers. They are among the best reported for mostly Sn-based perovskites[42,43] and significantly better than previous efforts based on vapor deposition.[44−46] Additionally, we found that the as-deposited films required no thermal annealing, minimizing the exposure of predeposited layers to elevated temperatures. This suggests that vapor deposition is a promising route for low-bandgap perovskites, and the process could be easily transferred into multijunction architectures.

On the basis of these insights, we expect that continued rational optimization of the precursor ratio should lead to improved film formation, particularly in the phase purity of the resulting perovskite. In addition, greater control over the film stoichiometry is required, which we expect to achieve through further understanding of the decomposition of the individual precursors within the starting mixtures. A significant portion of the parameter space within our current approach thus remains to be explored and is the subject of ongoing work.

In summary, we have demonstrated a new method of vapor deposition of perovskites that enables the formation of thin films with multiple cations in both the A- and B-sites from only two sources. This is enabled by the formation of unconventional mixtures of metal halides and ABX_3 precursor phases that can act as a single source of Cs, Pb, Sn, and some I. Incorporating SnF_2 substitutionally with SnI_2 in the mixture provides regulation of crystallization and the formation of impurity phases in the final perovskite films, which in turn determines their optoelectronic properties and device performance. In particular, the internal quantum efficiency for photoexcitation in the blue is quite sensitive to the SnF_2 content in the precursor mixture, which is the main limitation on device efficiency. Further optimization of the precursor mixture to suppress impurity phases and enable wider control over the final film stoichiometry should lead us toward highly efficient low-bandgap perovskite junctions suitable for all-perovskite multijunction cells formed by vapor deposition.

■ ASSOCIATED CONTENT

Supporting Information

The Supporting Information is available free of charge on the ACS Publications website at DOI: 10.1021/acsenergylett.9b01855.

Experimental methods and supplementary discussion, data, and figures and tables of X-ray diffraction, scanning electron microscopy, UV−vis−NIR absorption, steady-state PL, inductively coupled plasma mass spectroscopy, mobility and diffusion length calculations, spectral mismatch factor calculations, solar cell characterization, thickness measurements, estimation of bandgaps and limiting V_{OC}, and solution-processed films and devices (PDF)

■ AUTHOR INFORMATION

Corresponding Authors

*E-mail: michael.johnston@physics.ox.ac.uk.
*E-mail: henry.snaith@physics.ox.ac.uk.

ORCID

James M. Ball: 0000-0003-1730-5217
Juliane Borchert: 0000-0001-7973-6907
Laura M. Herz: 0000-0001-9621-334X
Michael B. Johnston: 0000-0002-0301-8033
Henry J. Snaith: 0000-0001-8511-790X

Notes

The authors declare the following competing financial interest(s): H.J.S. is the co-founder and CSO of Oxford PV Ltd, a company that is commercializing perovskite photovoltaic technologies.

■ ACKNOWLEDGMENTS

The authors would like to thank Dr. Bernard Wenger and Dr. Rebecca Sutton for helpful discussions and assistance with preliminary measurements. Additionally, we would like to thank Dr. Jessica Oliver of the Materials Innovation Factory, University of Liverpool for performing ICP-MS measurements. This work was supported by the UK Engineering and Physical Sciences Research Council (EPSRC) Grants EP/P006329/1 and EP/S516119/1. M.B.J. acknowledges support from the Humboldt Foundation. J.B. thanks the EPSRC for funding via the Centre for Doctoral Training in New and Sustainable Photovoltaics.

■ REFERENCES

(1) Lee, M. M.; Teuscher, J.; Miyasaka, T.; Murakami, T. N.; Snaith, H. J. Efficient Hybrid Solar Cells Based on Meso-Superstructured Organometal Halide Perovskites. *Science* **2012**, *338* (6107), 643−647.
(2) Kim, H.-S.; Lee, C.-R.; Im, J.-H.; Lee, K.-B.; Moehl, T.; Marchioro, A.; Moon, S.-J.; Humphry-Baker, R.; Yum, J.-H.; Moser, J. E.; et al. Lead Iodide Perovskite Sensitized All-Solid-State Submicron Thin Film Mesoscopic Solar Cell with Efficiency Exceeding 9%. *Sci. Rep.* **2012**, *2*, 591.
(3) Green, M. A.; Hishikawa, Y.; Dunlop, E. D.; Levi, D. H.; Hohl-Ebinger, J.; Yoshita, M.; Ho-Baillie, A. W. Y. Solar Cell Efficiency Tables (Version 53). *Prog. Photovoltaics* **2019**, *27* (1), 3−12.
(4) Martí, A.; Araújo, G. L. Limiting Efficiencies for Photovoltaic Energy Conversion in Multigap Systems. *Sol. Energy Mater. Sol. Cells* **1996**, *43* (2), 203−222.
(5) Eperon, G. E.; Hörantner, M. T.; Snaith, H. J. Metal Halide Perovskite Tandem and Multiple-Junction Photovoltaics. *Nat. Rev. Chem.* **2017**, *1* (12), 0095.

DOI: 10.1021/acsenergylett.9b01855
ACS Energy Lett. 2019, 4, 2748−2756

(6) Leijtens, T.; Bush, K. A.; Prasanna, R.; McGehee, M. D. Opportunities and Challenges for Tandem Solar Cells Using Metal Halide Perovskite Semiconductors. *Nat. Energy* **2018**, *3* (10), 828.
(7) Eperon, G. E.; Leijtens, T.; Bush, K. A.; Prasanna, R.; Green, T.; Wang, J. T.-W.; McMeekin, D. P.; Volonakis, G.; Milot, R. L.; May, R.; et al. Perovskite-Perovskite Tandem Photovoltaics with Optimized Band Gaps. *Science* **2016**, *354* (6314), 861−865.
(8) Forgács, D.; Gil-Escrig, L.; Pérez-Del-Rey, D.; Momblona, C.; Werner, J.; Niesen, B.; Ballif, C.; Sessolo, M.; Bolink, H. J. Efficient Monolithic Perovskite/Perovskite Tandem Solar Cells. *Adv. Energy Mater.* **2017**, *7* (8), 1602121.
(9) Leijtens, T.; Prasanna, R.; Bush, K. A.; Eperon, G. E.; Raiford, J. A.; Gold-Parker, A.; Wolf, E. J.; Swifter, S. A.; Boyd, C. C.; Wang, H.-P.; et al. Tin−Lead Halide Perovskites with Improved Thermal and Air Stability for Efficient All-Perovskite Tandem Solar Cells. *Sustain. Energy Fuels* **2018**, *2* (11), 2450−2459.
(10) Hörantner, M. T.; Leijtens, T.; Ziffer, M. E.; Eperon, G. E.; Christoforo, M. G.; McGehee, M. D.; Snaith, H. J. The Potential of Multijunction Perovskite Solar Cells. *ACS Energy Lett.* **2017**, *2* (10), 2506−2513.
(11) Zong, Y.; Wang, N.; Zhang, L.; Ju, M.-G.; Zeng, X. C.; Sun, X. W.; Zhou, Y.; Padture, N. P. Homogenous Alloys of Formamidinium Lead Triiodide and Cesium Tin Triiodide for Efficient Ideal-Bandgap Perovskite Solar Cells. *Angew. Chem., Int. Ed.* **2017**, *56* (41), 12658−12662.
(12) Wang, C.; Song, Z.; Li, C.; Zhao, D.; Yan, Y. Low-Bandgap Mixed Tin-Lead Perovskites and Their Applications in All-Perovskite Tandem Solar Cells. *Adv. Funct. Mater.* **2019**, 1808801.
(13) Tong, J.; Song, Z.; Kim, D. H.; Chen, X.; Chen, C.; Palmstrom, A. F.; Ndione, P. F.; Reese, M. O.; Dunfield, S. P.; Reid, O. G.; et al. Carrier Lifetimes of > 1 μs in Sn-Pb Perovskites Enable Efficient All-Perovskite Tandem Solar Cells. *Science* **2019**, *364* (6439), 475−479.
(14) Hao, F.; Stoumpos, C. C.; Chang, R. P. H.; Kanatzidis, M. G. Anomalous Band Gap Behavior in Mixed Sn and Pb Perovskites Enables Broadening of Absorption Spectrum in Solar Cells. *J. Am. Chem. Soc.* **2014**, *136* (22), 8094−8099.
(15) Leijtens, T.; Prasanna, R.; Gold-Parker, A.; Toney, M. F.; McGehee, M. D. Mechanism of Tin Oxidation and Stabilization by Lead Substitution in Tin Halide Perovskites. *ACS Energy Lett.* **2017**, *2* (9), 2159−2165.
(16) Lin, R.; Xiao, K.; Qin, Z.; Han, Q.; Zhang, C.; Wei, M.; Saidaminov, M. I.; Gao, Y.; Xu, J.; Xiao, M. Monolithic All-Perovskite Tandem Solar Cells with 24.8% Efficiency Exploiting Comproportionation to Suppress Sn(II) Oxidation in Precursor Ink. *Nat. Energy* **2019**, 1−10.
(17) McMeekin, D. P.; Sadoughi, G.; Rehman, W.; Eperon, G. E.; Saliba, M.; Hörantner, M. T.; Haghighirad, A.; Sakai, N.; Korte, L.; Rech, B.; et al. A Mixed-Cation Lead Mixed-Halide Perovskite Absorber for Tandem Solar Cells. *Science* **2016**, *351* (6269), 151−155.
(18) Liu, M.; Johnston, M. B.; Snaith, H. J. Efficient Planar Heterojunction Perovskite Solar Cells by Vapour Deposition. *Nature* **2013**, *501* (7467), 395−398.
(19) Momblona, C.; Gil-Escrig, L.; Bandiello, E.; Hutter, E. M.; Sessolo, M.; Lederer, K.; Blochwitz-Nimoth, J.; Bolink, H. J. Efficient Vacuum Deposited p-i-n and n-i-p Perovskite Solar Cells Employing Doped Charge Transport Layers. *Energy Environ. Sci.* **2016**, *9* (11), 3456−3463.
(20) Gil-Escrig, L.; Momblona, C.; La-Placa, M.-G.; Boix, P. P.; Sessolo, M.; Bolink, H. J. Vacuum Deposited Triple-Cation Mixed-Halide Perovskite Solar Cells. *Adv. Energy Mater.* **2018**, *8* (14), 1703506.
(21) Igual-Muñoz, A. M.; Ávila, J.; Boix, P. P.; Bolink, H. J. $FAPb_{0.5}Sn_{0.5}I_3$: A Narrow Bandgap Perovskite Synthesized through Evaporation Methods for Solar Cell Applications. *Sol. RRL* **2019**, DOI: 10.1002/solr.201900283.
(22) Milot, R. L.; Klug, M. T.; Davies, C. L.; Wang, Z.; Kraus, H.; Snaith, H. J.; Johnston, M. B.; Herz, L. M. The Effects of Doping Density and Temperature on the Optoelectronic Properties of Formamidinium Tin Triiodide Thin Films. *Adv. Mater.* **2018**, *30* (44), 1804506.
(23) Kuku, T. A.; Adeosun, O. S.; Akande, A. R.; Adiguzel, O. Transport Properties of PbSnI4. *Solid State Ionics* **1988**, *31* (1), 73−78.
(24) Kuku, T. A. Ion Transport Studies on Vacuum Deposited PbSnI4 Thin Films. *Thin Solid Films* **1999**, *340* (1), 292−296.
(25) Chung, I.; Song, J.-H.; Im, J.; Androulakis, J.; Malliakas, C. D.; Li, H.; Freeman, A. J.; Kenney, J. T.; Kanatzidis, M. G. CsSnI3: Semiconductor or Metal? High Electrical Conductivity and Strong Near-Infrared Photoluminescence from a Single Material. High Hole Mobility and Phase-Transitions. *J. Am. Chem. Soc.* **2012**, *134* (20), 8579−8587.
(26) Yamada, K.; Funabiki, S.; Horimoto, H.; Matsui, T.; Okuda, T.; Ichiba, S. Structural Phase Transitions of the Polymorphs of CsSnI3 by Means of Rietveld Analysis of the X-Ray Diffraction. *Chem. Lett.* **1991**, *20* (5), 801−804.
(27) Sutton, R. J.; Filip, M. R.; Haghighirad, A. A.; Sakai, N.; Wenger, B.; Giustino, F.; Snaith, H. J. Cubic or Orthorhombic? Revealing the Crystal Structure of Metastable Black-Phase CsPbI3 by Theory and Experiment. *ACS Energy Lett.* **2018**, *3* (8), 1787−1794.
(28) Kostko, V. S.; Kostko, O. V.; Makovetskii, G. I.; Yanushkevich, K. I. Thin Film Structure of Tin(II) Iodide. *Phys. Status Solidi B* **2002**, *229* (3), 1349−1352.
(29) Smakula, A.; Kalnajs, J. Precision Determination of Lattice Constants with a Geiger-Counter X-Ray Diffractometer. *Phys. Rev.* **1955**, *99* (6), 1737−1743.
(30) Stoumpos, C. C.; Malliakas, C. D.; Kanatzidis, M. G. Semiconducting Tin and Lead Iodide Perovskites with Organic Cations: Phase Transitions, High Mobilities, and Near-Infrared Photoluminescent Properties. *Inorg. Chem.* **2013**, *52* (15), 9019−9038.
(31) Tauc, J. Optical Properties and Electronic Structure of Amorphous Ge and Si. *Mater. Res. Bull.* **1968**, *3* (1), 37−46.
(32) Elliott, R. J. Intensity of Optical Absorption by Excitons. *Phys. Rev.* **1957**, *108* (6), 1384−1389.
(33) Saba, M.; Cadelano, M.; Marongiu, D.; Chen, F.; Sarritzu, V.; Sestu, N.; Figus, C.; Aresti, M.; Piras, R.; Geddo Lehmann, A.; et al. Correlated Electron−Hole Plasma in Organometal Perovskites. *Nat. Commun.* **2014**, *5*, 5049.
(34) Galkowski, K.; Mitioglu, A.; Miyata, A.; Plochocka, P.; Portugall, O.; Eperon, G. E.; Wang, J. T.-W.; Stergiopoulos, T.; Stranks, S. D.; Snaith, H. J.; et al. Determination of the Exciton Binding Energy and Effective Masses for Methylammonium and Formamidinium Lead Tri-Halide Perovskite Semiconductors. *Energy Environ. Sci.* **2016**, *9* (3), 962−970.
(35) Milot, R. L.; Eperon, G. E.; Green, T.; Snaith, H. J.; Johnston, M. B.; Herz, L. M. Radiative Monomolecular Recombination Boosts Amplified Spontaneous Emission in HC(NH2)2SnI3 Perovskite Films. *J. Phys. Chem. Lett.* **2016**, *7* (20), 4178−4184.
(36) Patel, J. B.; Wong-Leung, J.; Van Reenen, S.; Sakai, N.; Wang, J. T. W.; Parrott, E. S.; Liu, M.; Snaith, H. J.; Herz, L. M.; Johnston, M. B. Influence of Interface Morphology on Hysteresis in Vapor-Deposited Perovskite Solar Cells. *Adv. Electron. Mater.* **2017**, *3* (2), 1600470.
(37) Borchert, J.; Milot, R. L.; Patel, J. B.; Davies, C. L.; Wright, A. D.; Martínez Maestro, L.; Snaith, H. J.; Herz, L. M.; Johnston, M. B. Large-Area, Highly Uniform Evaporated Formamidinium Lead Triiodide Thin Films for Solar Cells. *ACS Energy Lett.* **2017**, *2* (12), 2799−2804.
(38) Snaith, H. J.; Abate, A.; Ball, J. M.; Eperon, G. E.; Leijtens, T.; Noel, N. K.; Stranks, S. D.; Wang, J. T.-W.; Wojciechowski, K.; Zhang, W. Anomalous Hysteresis in Perovskite Solar Cells. *J. Phys. Chem. Lett.* **2014**, *5* (9), 1511−1515.
(39) Rohatgi, A. WebPlotDigitizer, v4.2. https://automeris.io/WebPlotDigitizer (2019).
(40) Lin, Q.; Armin, A.; Burn, P. L.; Meredith, P. Filterless Narrowband Visible Photodetectors. *Nat. Photonics* **2015**, *9* (10), 687−694.

DOI: 10.1021/acsenergylett.9b01855
ACS Energy Lett. 2019, 4, 2748−2756

(41) Rau, U.; Blank, B.; Müller, T. C. M.; Kirchartz, T. Efficiency Potential of Photovoltaic Materials and Devices Unveiled by Detailed-Balance Analysis. *Phys. Rev. Appl.* **2017**, *7* (4), 044016.
(42) Shao, S.; Liu, J.; Portale, G.; Fang, H.-H.; Blake, G. R.; ten Brink, G. H.; Koster, L. J. A.; Loi, M. A. Highly Reproducible Sn-Based Hybrid Perovskite Solar Cells with 9% Efficiency. *Adv. Energy Mater.* **2018**, *8* (4), 1702019.
(43) Ke, W.; Stoumpos, C. C.; Kanatzidis, M. G. "Unleaded" Perovskites: Status Quo and Future Prospects of Tin-Based Perovskite Solar Cells. *Adv. Mater.* **2018**, *0* (0), 1803230.
(44) Jung, M.-C.; Raga, S. R.; Qi, Y. Properties and Solar Cell Applications of Pb-Free Perovskite Films Formed by Vapor Deposition. *RSC Adv.* **2016**, *6* (4), 2819−2825.
(45) Yu, Y.; Zhao, D.; Grice, C. R.; Meng, W.; Wang, C.; Liao, W.; Cimaroli, A. J.; Zhang, H.; Zhu, K.; Yan, Y. Thermally Evaporated Methylammonium Tin Triiodide Thin Films for Lead-Free Perovskite Solar Cell Fabrication. *RSC Adv.* **2016**, *6* (93), 90248−90254.
(46) Moghe, D.; Wang, L.; Traverse, C. J.; Redoute, A.; Sponseller, M.; Brown, P. R.; Bulović, V.; Lunt, R. R. All Vapor-Deposited Lead-Free Doped CsSnBr3 Planar Solar Cells. *Nano Energy* **2016**, *28*, 469−474.

DOI: 10.1021/acsenergylett.9b01855
ACS Energy Lett. 2019, 4, 2748−2756